CHEMISTRY OF MATERIALS

pubs.acs.org/cm

Article

Porous Metals from Chemical Dealloying for Solid-State Battery Anodes

Sang Yun Han, John A. Lewis, Pralav P. Shetty, Jared Tippens, David Yeh, Thomas S. Marchese, and Matthew T. McDowell*

Cite This: https://dx.doi.org/10.1021/acs.chemmater.9b04992

Read Online

ACCESS | Metrics & More | Article Recommendations | Supporting Information

ABSTRACT: Alloy anodes for lithium-ion batteries feature greater specific capacity than conventional graphite electrodes and could enable batteries with higher energy density. However, large volumetric and structural changes during cycling limit performance. Such transformations are expected to be particularly problematic in solid-state batteries, where volume changes can exacerbate chemomechanical degradation of the all-solid structure. Here, we synthesize porous metal foils with bicontinuous porosity by chemical dealloying of Li−In and Li−Sn alloys in dry methanol. Porous indium foils are directly used as the anode in both solid-state and liquid-electrolyte cells, and they exhibit improved capacity and cycle life in solid-state batteries compared to dense indium foil with similar mass loading. Furthermore, capacity retention with cycling of the porous electrodes is much better in solid-state cells than in liquid cells. This performance enhancement is due to improved accommodation of volume changes while minimizing surface side reactions throughout the porous electrode. These results highlight the promise of porous metals for solid-state batteries.

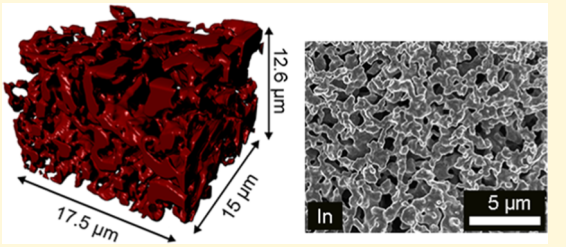

INTRODUCTION

Porous metal structures are of technological interest for a variety of applications, including electrocatalysis,[1] multifunctional structural elements,[2] military armor,[3] supercapacitors,[4] radiation shielding,[5] actuators,[6] and sensors.[7] Porous metals have also shown promising electrochemical behavior as electrode materials that exhibit alloying reactions in liquid-electrolyte batteries.[8−10] These applications benefit from the advantageous properties of porous metals, such as a high surface area per volume, relatively simple fabrication techniques, and improved mechanical behavior.[11,12] Many such properties (such as enhanced yield strength, high specific surface area, and low density) only arise when the ligaments that create the structural framework of a porous metal are smaller than a few microns. Thus, techniques for synthesizing a wide variety of porous metals with a controlled nano-to-micron-scale pore size are necessary.

Selective dealloying has been one of the most successful routes for producing metals with small-scale porosity.[13−15] Dealloying of binary alloys containing noble metals, such as Ag−Au or Cu−Au, has been extensively studied. These materials can form a bicontinuous ligament morphology with uniform ligament size of a few hundred nanometers upon (electro)chemical dealloying of the more reactive element. However, conventional dealloying methods are only useful for creating porous noble metals due to the chemistries utilized. As an alternative option, dealloying of Li-rich alloy materials has emerged in recent years as a route to porous metals other than the noble variety.[8] Lithium forms alloys with a wide variety of other metals at relatively low temperatures, and the high diffusivity of Li in many materials readily enables alloy formation. Previously, porous Sn structures were created by electrochemical dealloying of lithium from Li−Sn alloys,[8] and this study showed that the nature of the porosity could be controlled as a function of Li removal rate. Furthermore, there has been a number of recent studies in which lithium was used as a processing agent to form other porous or nanostructured materials,[16−18] such as Al alkoxide nanowires created by dealloying of Al.[18] The large quantity of Li-rich alloys and the versatility of these techniques could enable the synthesis of new porous and nanostructured metals for a variety of applications.

Metals that form alloys with Li also have great promise for use as high-capacity anodes within Li-based battery systems.[19−23] Metals such as Sn, In, Sb, and Si can electrochemically react to form Li-rich alloys at room temperature, such as $Li_{22}Sn_5$, $Li_{13}In_3$, Li_3Sb, and $Li_{15}Si_4$.[8,24−27] These materials have higher specific capacities than conventional graphite anodes (e.g., 990 mAh g^{-1} for Sn and 1012 mAh g^{-1} for In, as compared to 372 mAh g^{-1} for graphite),[9,24] and they also exhibit very high volumetric capacities (e.g., 1991 mAh cm^{-3}

Received: December 3, 2019
Revised: February 26, 2020
Published: February 26, 2020

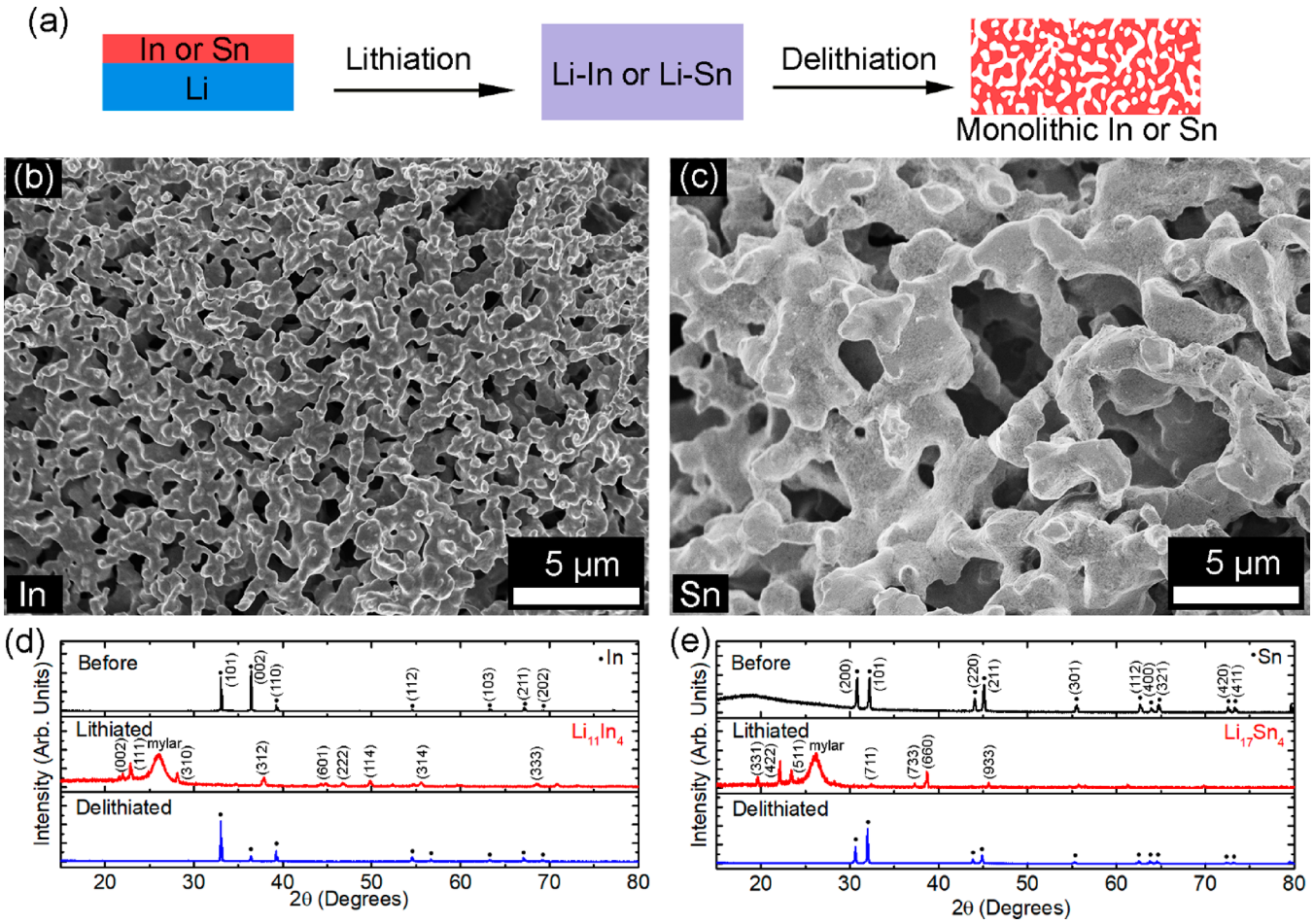

Figure 1. Synthesis and characterization of porous metals by chemical dealloying. (a) Schematic showing the synthesis of porous In or Sn foil via the delloying of a Li−In or Li−Sn alloy (a Li:In or Li:Sn molar ratio of 5:1 was used). (b) SEM image of a dealloyed In sample. (c) SEM image of a dealloyed Sn sample. (d, e) XRD patterns of In (d) and Sn (e) samples at different steps of the synthetic procedure.

for Sn and 1980 mAh cm^{-3} for In, as compared to 330−430 mAh cm^{-3} for graphite).[28] Substantial research effort has been specifically devoted to incorporating Si into liquid-electrolyte batteries due to its high capacity and natural abundance.[29,30] A longstanding issue with these materials, however, is that electrochemical Li insertion and extraction cause significant volumetric and structural changes,[31,32] which can result in fracture and chemomechanical degradation.[33] In addition, the freshly exposed surface area due to cracks can form new solid-electrolyte interphase (SEI) films when using liquid electrolytes, reducing Coulombic efficiency during cycling.[34]

Despite their challenges, metallic alloy anodes may hold particular promise for emerging solid-state battery (SSB) systems that utilize inorganic solid-state electrolytes (SSEs). Using Li metal anodes within SSBs would be ideal due to the ultrahigh capacity of Li, but fundamental issues with interfacial instabilities at Li metal/SSE interfaces, as well as Li filament growth through many SSEs, have not yet been overcome.[35−37] Alloy anodes offer high capacity and a higher electrode potential than pure Li metal, and there is evidence that they may allow for improved interfacial stability.[38] However, new challenges are expected to arise when implementing large-volume-change alloy electrodes within SSBs: in particular, volume changes of the electrode material are expected to cause exacerbated mechanical degradation due to the all-solid nature of the battery.[35,39] Indeed, mechanical fracture and degradation have recently been observed in Sn-based anodes in SSBs.[40] Thus, new methods for implementing alloy anodes designed for minimal chemomechanical degradation within SSBs are necessary.

Here, we report the synthesis of In and Sn foil structures with bicontinuous porosity and demonstrate that porous In exhibits promising electrochemical characteristics within SSBs. The porous metal foils are created by free-corrosion dealloying of Li-rich alloys within dry methanol. Structural characterization of the porous In material reveals a pore fraction of 0.68 and a ligament size of less than 2 μm. The porous In foils were used directly as battery electrodes without any additive or binder within both liquid cells and solid-state cells with $Li_{10}SnP_2S_{12}$ (LSPS) solid-state electrolyte. This material exhibits higher specific capacity and better cycle life compared to dense In foil within SSBs, which is likely due to the free volume that allows for expansion and the continuous electrically conducting network. Our results show that porous metal anodes could enable high capacity and extended cycle life within SSBs.

RESULTS AND DISCUSSION

We fabricated porous metal foils with bicontinuous ligaments and porosity by chemical dealloying (free corrosion) of Li from bulk Li−In and Li−Sn alloys. Figure 1a shows a schematic of this process. To synthesize Li-rich alloys, an In or Sn metal

https://dx.doi.org/10.1021/acs.chemmater.9b04992
Chem. Mater. XXXX, XXX, XXX−XXX

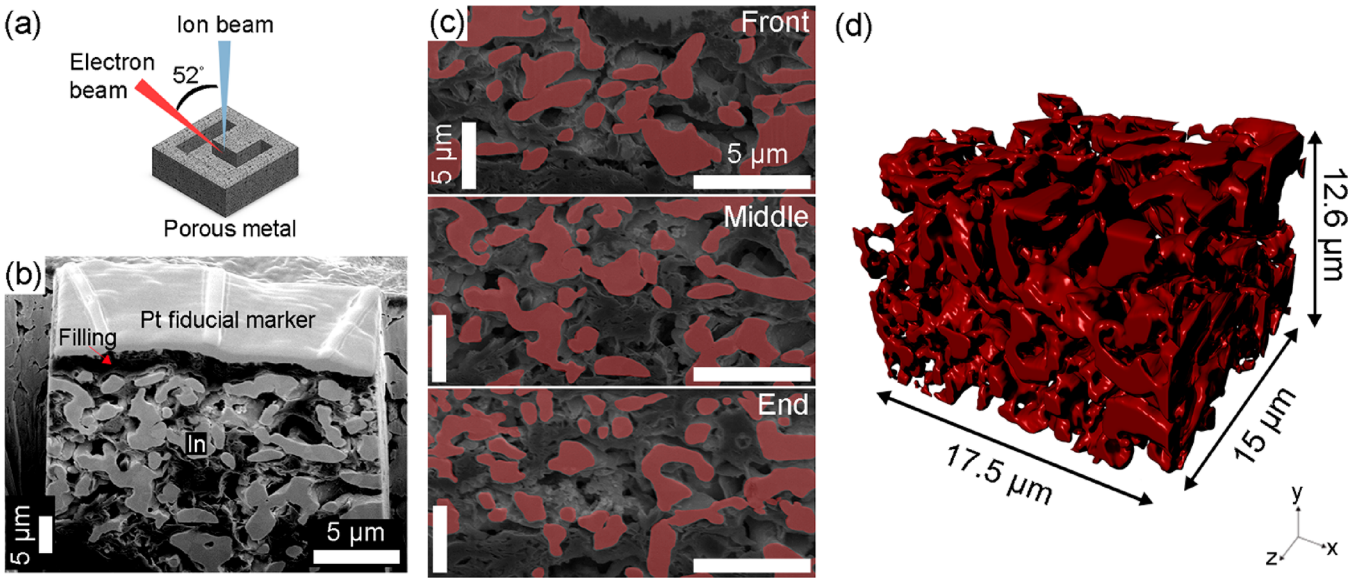

Figure 2. Physical characterization of the porous In. (a) Schematic showing the FIB tomography experiment and trench geometry used for this measurement. (b) An SEM image of the front surface of the milled porous In sample with carbon infill. (c) Segmented SEM images of the front, middle, and end slices of the milled volume, in which the artificial red overlay is the segmented metallic phase. (d) Full 3D tomographic reconstruction of the porous In sample.

pellet was first created by uniaxially pressing the metal powder, and this pellet was then sandwiched with Li foil using a molar ratio of 5:1 (Li:In or Li:Sn). These layered samples were heated at relatively low temperatures (220−230 °C) for 4 h inside an Ar-filled glovebox to form the Li−In or Li−Sn alloys. After alloying, the alloy foils were then submerged in dry methanol at 60 °C to extract Li. This synthesis process reliably and reproducibly caused the formation of porous foils, as shown in the scanning electron microscopy (SEM) images of the In and Sn samples in Figure 1b,c. Figures S1 and S2 in the Supporting Information (SI) contain an optical image of the porous foil obtained from a Li−In sample and additional low-magnification SEM images of the porous materials.

Structural characterization revealed that the In and Sn samples exhibited consistent ligament size at different locations on the samples. The average widths of the ligaments from SEM imaging were measured to be 700 ± 210 nm for In and 1.80 ± 0.37 μm for Sn. X-ray diffraction (XRD) was used to investigate the evolution of structure during the synthetic procedure, as shown in Figure 1d,e. XRD of the pristine In and Sn samples before alloying showed the expected tetragonal crystal structures. After chemical alloying, the detected phases are primarily $Li_{11}In_4$ (ICDD 04-021-2444, space group $C2/m$) and $Li_{17}Sn_4$ (ICDD 04-014-6237, space group $F\bar{4}32m$). Li_2O or Li peaks were not detected. The broad peaks between 25 and 30° in the lithiated samples arise from the mylar film used to protect the lithiated samples from oxidation during XRD measurements. After Li removal, the materials returned to the original metallic phases. The change in peak intensities is attributed to microstructural changes during the transformation from a dense pellet to a porous structure. No Li or Li_2O was detected after dealloying; this indicates that the Li was completely removed from the Li alloys after delithiation.

The dealloying of Li-rich alloys with other metals, such as Bi, Sb, Ag, and Au, was also investigated, but these materials did not form a porous morphology like In or Sn under these conditions (Figure S3). Au and Ag showed cracks after delithiation, and Sb was pulverized to smaller particles. Bi retained its bulk foil form with embedded porosity (Figure S3). These findings suggest that different reactions and lithium diffusion kinetics within these alloys could play an important role in determining the final morphology. Experiments with In pellets were carried out to examine the effect of alloy molar ratio on the final porous structure. Porous ligamentary structures were observed at least partially for Li:In molar ratios greater than 2:1 (Figure S4). In addition, further experiments with dealloying time as a variable showed that porous structures form after dealloying for at least 2 h at 60 °C (Figure S5). After 6 h, ligaments with improved uniformity were observed, which could be due to the continued diffusion of Li out of the monolith. Dealloying for 48 h did not significantly change the ligament morphology.

The creation of these porous metals via dealloying of Li is consistent with a handful of previous studies on using lithium as a processing agent. Recently, reactions between Li−Al alloys and dry ethanol were studied,[18] which resulted in the formation of Al alkoxide nanowires due to the reaction of Al with ethanol. In our case, both Sn and In were observed to form porous metallic structures rather than oxides, which is likely due to the reduced tendency of these metals to oxidize compared to Al. In addition, Li-rich Li−Sn particles have been shown to form porous morphologies during electrochemical dealloying at high currents.[8] This study found that a fast dealloying rate was necessary for forming porous, bicontinuous structures. This is because the Li dissolution rate has to be fast enough to minimize surface diffusion smoothening, which causes Li redistribution that can prevent pore formation. The chemical corrosion in our experiments causes fast enough dealloying rates to overcome internal Li redistribution for the formation of bicontinuous structures. For comparison to chemical dealloying, we performed electrochemical dealloying experiments, as shown in Figures S6 and S7. In these experiments, In pellets were electrochemically lithiated and delithiated in coin cells at current densities ranging from 0.3 to 2.0 mA cm^{-2} followed by characterization of the morphology of the different pellets. This electrochemical delithiation of the

https://dx.doi.org/10.1021/acs.chemmater.9b04992
Chem. Mater. XXXX, XXX, XXX−XXX

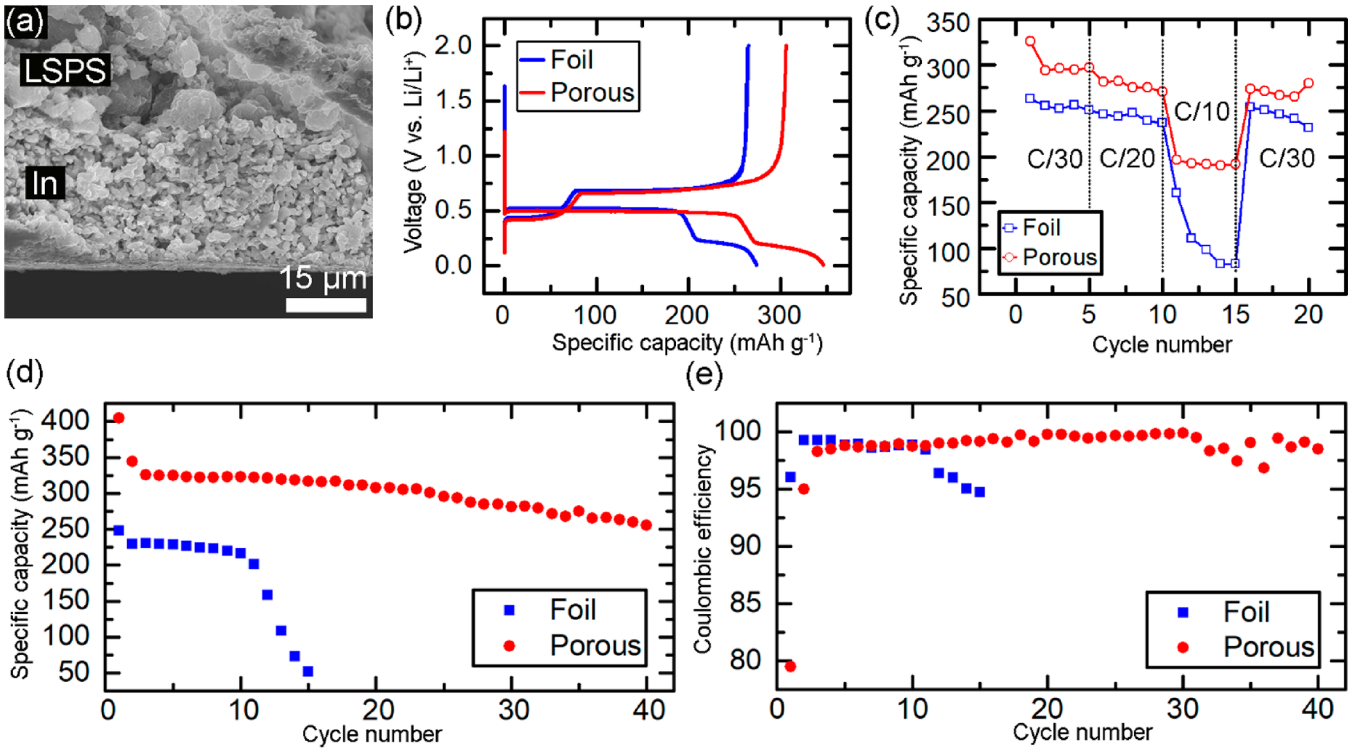

Figure 3. Porous In electrodes within solid-state batteries. (a) Cross-sectional SEM image of a porous In electrode that was pressed within a solid-state cell and removed for imaging. (b) First galvanostatic lithiation/delithiation of a porous In sample and a dense In foil sample. The current density was 0.60 mA cm^{-2} for the dense foil and 0.69 mA cm^{-2} for the porous electrode. Both electrodes had mass loadings between 1 and 2 mg, and lithium foil was used as the counter electrode. (c) Rate capability of a porous In electrode and a dense In foil electrode within solid-state cells at various rates from C/30 to C/10 (1C = 1012 mA g^{-1} of In). Lithium foil was used as the counter electrode. (d) Capacity retention with cycling for a porous electrode and a dense foil electrode at a rate of C/20 (0.75 mA cm^{-2}). For long-term stability, these cells included a thick In metal foil in contact with the Li counter electrode to reduce interfacial degradation of the SSE (see Experimental Section). (e) Coulombic efficiency from the cells in (d).

Li−In alloy did not result in a porous structure as observed from chemically dealloying; this difference was likely a result of the lower dealloying rates used in electrochemical Li removal. Importantly, the relatively large mass of the metal pellet (~2 mg) will likely make it impossible to sustain a high enough electrochemical dealloying rate for the formation of bicontinuous porosity in the full pellet, and thus the free-corrosion dealloying is essential for creating the porous structure.

The pore and ligament structures of a chemically dealloyed In sample were further characterized with focused ion beam (FIB) tomography. Figure 2a shows a schematic of the FIB tomography experiment, where there was an angle of 52° between the milling ion beam and the imaging electron beam. Carbon paste was used to fill in the pores of the sample and to prevent small ligaments from breaking during tomography (see Experimental Section for details). Figure 2b shows a single image from the experiment, and Figure 2c shows image slices from different depths, along with the segmented metallic regions overlaid in red. The full 3D reconstruction of the metallic phase within a ~3307 μm^3 volume is shown in Figure 2d. The data in Figure 2 show that the average ligament width in this volume is 850 nm, which is slightly larger than the value measured directly from SEM images. In addition, voids were not observed within the In ligaments. Within this 3307 μm^3 external volume, the measured internal volume of the In metal was 1055 μm^3, and the surface area was 3903 μm^2. This value of the surface area is 2.9 times that of a dense metal foil. The pore volume of the material was 68% of the total volume. Other regions within the same sample were similarly characterized using FIB tomography and showed similar results. Finally, the pore tortuosity of the segmented volume in Figure 2d was analyzed using Dragonfly software. Tortuosity quantitatively describes transport pathways through a given phase, and it is defined as $\tau = L_{eff}/L$, where L_{eff} is the length of a curvilinear path through a structure, and L is the Euclidean distance through the structure.[41,42] A tortuosity of 1.60 was measured for the segmented volume in Figure 2.

The porous In electrodes were investigated as anodes for SSBs. Solid-state battery cells with a lithium counter electrode were constructed using a custom cell assembly inside an Ar-filled glovebox (the Experimental Section contains complete details). $Li_{10}SnP_2S_{12}$ (LSPS) was used as the solid-state electrolyte (SSE) due to its high ionic conductivity and relatively stable interface with Li alloys.[43] The In electrodes were not mixed with any conductive additives, binders, or SSE materials; instead, the porous In foils were placed directly in contact with the SSE. Figures 3a and S8 show cross-sectional SEM images of porous electrodes after being pressed into the battery assembly but before any electrochemical testing. From these images, it is clear that the internal porosity and ligaments within the structure are preserved even after being pressed at 15 MPa within the solid-state cell assembly, and the thickness of the porous In electrode was ~25 μm. The electrochemical characteristics of the In electrodes were evaluated using galvanostatic measurements using an indium working electrode and lithium foil counter electrode. Current densities between

https://dx.doi.org/10.1021/acs.chemmater.9b04992
Chem. Mater. XXXX, XXX, XXX−XXX

0.60 and 0.75 mA cm^{-2} were used over a voltage range of 0.01−2.0 V vs Li/Li^+ (this corresponds to a current of C/20 based on the mass and theoretical specific capacity of In). Figure 3b shows the first discharge and charge of a porous electrode compared to a cell with a dense foil working electrode with a similar mass loading. Both materials showed a first lithiation plateau at 0.5 V and a second at 0.25 V, and these plateaus were also visible during charge. The porous electrode had a specific capacity of 350 mAh g^{-1}, while the foil had a specific capacity of 270 mAh g^{-1} for the first discharge; thus, the porous electrode showed ∼1.3 times higher specific capacity than the dense foil. Both the In porous electrode and the dense foil attained lower capacities than theoretically possible (1012 mAh g^{-1}) because they did not access the lower plateau at 0.05 V, which has previously only been observed with a low current density of 50 μA cm^{-2} in liquid cells.[24]

The rate behavior and long-term cycling characteristics of these materials were investigated next. The rate behavior of the electrode materials was tested at various rates from C/30 to C/10 (1C = 1012 mA g^{-1} of In), and reduced capacity was observed at C/10 (Figure 3c). At all currents, the porous In electrodes exhibit higher capacity than the dense foil. Figure 3d shows the capacity retention with cycling for a porous In electrode vs a dense foil electrode over 40 cycles at a current of C/20. In this configuration, the porous electrode exhibited a higher first-discharge specific capacity of 408 mAh g^{-1} compared to the dense foil (250 mAh g^{-1}). The porous electrode also featured better capacity retention (a decrease from 408 to 300 mAh g^{-1} over 40 cycles) compared to the dense foil, which experienced steep capacity decay after 10 cycles. The Coulombic efficiency (CE) of the porous electrode increased from 80.0% in the first cycle to an average value of 98.5% over 40 cycles, while the dense In foil featured an initial CE of 94.0% with an average value of 97.7% over 15 cycles. In these longer-term cycling tests (Figure 3d,e), we note that the counter electrodes consisted of a 50 μm thick In foil placed at the interface between the SSE and the Li metal to improve chemical stability of the SSE during cycling,[38] which limited SSE degradation and provided a better indication of the electrochemical stability of the In working electrodes themselves. Figures S9 and S10 show galvanostatic voltage curves, comparing the behavior of these In working electrodes coupled with either pure Li metal counter electrodes or In−Li counter electrodes. The overpotential steadily increased with cycling when using a pure Li counter electrode, but the use of the In−Li counter electrode prevented this degradation. Finally, we note that the higher observed capacity and better cycle life of the porous In material were observed consistently over multiple cells, with more data shown in Figure S11.

The improved capacity and cycle life of the porous metal electrodes are likely due to the capability of the porous material to accommodate the volume changes during lithiation/delithiation while minimizing mechanical damage of the cell stack and retaining electron transport pathways. Electrode volume changes can have particularly severe effects on the chemomechanical stability of solid-state batteries[35] since there is no liquid phase (as in conventional batteries) that can accommodate lithiation-induced strains. The built-in porosity of our metal electrodes thus allows for higher capacity and likely results in lower stresses within the rest of the cell stack. Interestingly, the porous material has the added advantage that it also exhibits higher capacity than the dense foil when cycled at higher current densities (Figure 3c), which may result from higher diffusion rates of the Li species on the surface of the metal ligaments compared to that within the bulk of the material. These results show that multiple features of porous metals enable improved performance in SSBs.

SEM and X-ray energy-dispersive spectroscopy (EDS) investigation of solid-state cells after one lithiation/delithiation cycle showed that the porous In retained its particulate structure, with porosity still evident between particles (Figures S12 and S13). This is in contrast to the dense foil electrodes, which did not evolve porosity after one cycle (Figures S14 and S15). The retention of the particulate structure likely enables continued higher specific capacity over further cycling, as shown in Figure 3. Additional information was gathered through SEM imaging of the cells in Figure 3 that were cycled to failure. Figures S16 and S17 show that the In foil remains dense but that the porous In electrode exhibits particle agglomeration with less evident porosity. Based on these data, it is possible that the gradual sintering between In ligaments during charge/discharge causes capacity decay over long periods.

We also examined the electrochemical behavior of the porous electrodes in conventional liquid-electrolyte cells. Half-cells were used with Li as the counter electrode, and we compared the electrochemical behavior of porous electrodes and dense foil. We utilized a carbonate-based electrolyte with a mixture of ethyl methyl carbonate (EMC), ethylene carbonate (EC), fluoroethylene carbonate (FEC), and $LiPF_6$ salt (see Experimental Section). FEC is necessary to prevent anomalous electrolyte decomposition on In electrodes, as has been previously reported.[24] A current density of 0.65 mA cm^{-2} and an active mass loading of 1−2 mg were used in coin cells for porous electrodes and foil over a voltage range from 0.01 to 2.0 V vs Li/Li^+. Figure S18 shows cross-sectional SEM images of porous and foil electrodes after being pressed inside the coin cell but before any electrochemical testing; these images show that the porous structure of the dealloyed electrodes remains after pressing.

Figure 4a,b shows galvanostatic tests over 15 cycles for dense In foil and porous electrodes, respectively. These data show that the porous electrode exhibits a higher specific capacity than the dense foil, which was consistent across multiple cells. During the first lithiation of the dense foil, the electrode potential was depressed below the expected plateau of 0.5 V vs Li/Li^+. The first lithiation of the porous electrode did not feature this lowered voltage, and it was also not observed in the solid-state testing of the dense In foil (Figure 3b) with similar mass loadings. The lowered initial discharge potential in Figure 4a may be due to a combination of a lower surface area of the dense foil compared to that of the porous sample and higher charge-transfer resistance in the liquid compared to that in the solid (Figures 4d and S19 show impedance spectra for both cases). From the 1st to the 10th cycle, the specific capacity of the dense foil had an average value of 247 mAh g^{-1} (Figure 4a), while the porous electrode had a higher average specific capacity of 432 mAh g^{-1} (Figure 4b). However, the capacity of the porous electrode decayed faster than that of the foil in these liquid cells, which is the opposite of the solid-state case (Figure S20). The morphology of the electrochemically lithiated and delithiated porous electrode samples is shown in Figure S21; the lithiated material features less visible porosity. Porosity returns after delithiation, but the ligaments seem to agglomerate to cause the particle size to be larger. Rate sensitivity tests were

https://dx.doi.org/10.1021/acs.chemmater.9b04992
Chem. Mater. XXXX, XXX, XXX−XXX

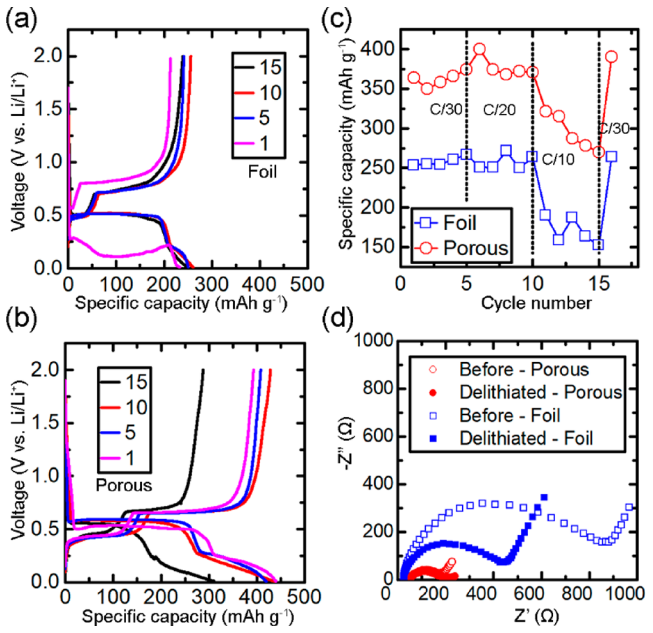

Figure 4. Porous In electrodes within liquid-cell batteries. (a, b) The 1st (pink), 5th (blue), 10th (red), and 15th (black) discharge/charge curves from half-cells with dense In foil (a) or porous In foil (b) working electrodes tested at C/20 (current density of 0.65 mA cm^{-2}). (c) Rate capability of porous In and dense In foil within half-cells at various rates from C/30 to C/10 (1C = 1012 mA g^{-1} of In). (d) Nyquist plots showing the impedance spectra before and after one discharge/charge cycle for each type of electrode.

performed for both types of electrodes in the liquid electrolyte, as shown in Figure 4c. These experiments showed that porous electrodes exhibited higher specific capacity across the range of rates from C/30 to C/10, which is a similar result to the solid-state case. Figure 4d shows electrochemical impedance spectroscopy (EIS) results. The charge-transfer resistance before cycling for the porous In electrode was 265 Ω, which is lower than the value of 880 Ω for the dense In foil. This is likely due to the increased surface area of the porous material, and the surface area ratio of 2.9 measured with FIB tomography correlates well with these different charge-transfer resistance values. After one cycle, the charge-transfer resistance decreased to 147 and 444 Ω for the porous and dense foil electrodes, respectively. This decrease could be due to a stable SEI formed on the surface of the electrodes.

The specific capacity attained using the porous In electrodes was superior to that of dense In foil in both solid-state and liquid-electrolyte cells. Furthermore, the porous electrodes showed long cycle life in solid-state cells but failed faster in the liquid cells than dense In foil. After the ∼15th cycle in liquid cells, capacity decay was severe for the porous electrodes. This is likely due to the continuous growth of SEI on the higher surface area of the porous electrodes, which can eventually impede ion transport. In solid-state cells, the higher surface area of the porous material enables improved accommodation of volume changes, while the interface with the SSE is confined to only a small portion of the porous material. Thus, an SEI does not grow to cover the entire surface area of the porous In but instead only covers a planar interface. The bulk and surface of the porous In materials allow for Li diffusion at a rate that is fast enough to support the currents used herein, and a liquid electrolyte is thus not needed to infiltrate the structure. This advantageous geometry improves cycling stability while also allowing for high capacity.

CONCLUSIONS

We have reported a new method to create porous In and Sn metal foils via the chemical dealloying of Li-rich alloys and have demonstrated the beneficial electrochemical characteristics of porous In for use in SSBs. In testing of solid-state cells, the porous In electrodes showed better rate behavior, higher specific capacity, and longer cycle life than dense In foil. Importantly, the cycling stability of the porous In within solid-state cells was superior to both dense foils in solid-state cell and porous In within liquid cells, which demonstrates the advantages of using porous metal in SSBs. Future work is needed to understand the interfacial evolution and stability of various SSE materials in contact with Li alloys, such as the Li−In alloy used here. Furthermore, it would be beneficial to develop and investigate other porous alloy anodes that exhibit even higher specific capacity than In. With additional effort and research, metals with tailored porosity could be utilized to enable next-generation solid-state batteries with a high specific energy.

EXPERIMENTAL SECTION

Synthesis of Porous In and Sn Electrodes. To fabricate the alloyed foil, In and Sn microparticles (Sigma-Aldrich, 99.9%) were compressed at 250 MPa into thin pellets using a hydraulic press. These pellets were then removed and physically pressed onto the top of Li metal foil (Sigma-Aldrich, 99.9%) inside an Ar-filled glovebox (MBraun) with H_2O and O_2 levels less than 2.0 ppm. Li metal foil was manually polished to remove the surface oxide layer in the glovebox before pressing. A molar ratio of 5:1 (Li:M, where M = In or Sn) was used for reaction with lithium. The samples were heated in a machined stainless steel boat on a hot plate within the glovebox at 220−230 °C for 4 h. A Signstek 6802 II dual channel digital thermometer with a K-type thermocouple was used to measure the temperature of the samples. After alloying, Li−In or Li−Sn alloys were chemically dealloyed by first immersing in anhydrous methanol (Alfa Aesar, 99.9%) inside the glovebox. Then, the immersed sample was taken out of the glovebox and placed on a hot plate, where it was heated at 60 °C for 8 h to facilitate dealloying. The sample was then rinsed with clean anhydrous methanol 3 times in the fume hood. Other experiments were carried out with varying dealloying temperatures and times.

Cell Fabrication and Electrochemistry. The electrochemical behavior of the produced materials was tested using CR2032 stainless steel coin cells (MTI Corp.) for liquid cells or a custom-built solid-state cell assembly shown in Figure S22. Galvanostatic electrochemical tests were performed on either a Bio-Logic VMP-3 potentiostat or a Landt CT2001 battery test system.

For coin cells, stainless steel current collectors (diameter = 15 mm) were used. Active material mass loadings of 1−3 mg for both porous In electrodes and dense In foils were used. Indium metal foil (50 μm, 99.99%, GalliumSource) was thinned to ∼20 μm using a roll press. Celgard polypropylene/polyethylene membranes were soaked in the electrolyte and used as separators. Lithium metal foil (Sigma-Aldrich, 99.9%) was used as a counter electrode after removing the surface contamination layer. The coin cells were assembled and pressed using a hydraulic press at 600 psi inside an Ar-filled glovebox. The electrolyte consisted of 1.0 M $LiPF_6$ in 0.5:0.3:0.2 ethyl methyl carbonate (EMC, Sigma-Aldrich, 99.9%): ethylene carbonate (EC, Sigma-Aldrich, 99%): fluoroethylene carbonate (FEC, Alfa Aesar, 98%). Galvanostatic half-cell cycling was performed at room temperature with voltage limits of 2.0 and 0.01 V vs Li/Li^+. The impedance measurements were performed on a Bio-Logic VMP3 potentiostat at frequencies between 1 MHz and 1 Hz using a 5 mV signal amplitude.

https://dx.doi.org/10.1021/acs.chemmater.9b04992
Chem. Mater. XXXX, XXX, XXX−XXX

For SSB cells, 180 mg of $Li_{10}SnP_2S_{12}$ powder (LSPS, NEI corporation) was pressed into a pellet (diameter = 10 mm) with a pressure of 63 MPa using a hydraulic press inside an Ar-filled glovebox. Active material mass loadings of 1−2 mg for porous In electrodes and dense In foil electrodes were used. The working electrode was placed on top of the compacted LSPS pellet, and a Li or Li/In counter electrode was placed on the other side. The assembly was then uniaxially compressed to 16.5 MPa using a torque wrench to ensure contact between electrodes and the electrolyte. To minimize deterioration of the Li/LSPS interface for long-term cycling tests, an additional In foil (50 μm thick) was placed between the Li foil and the LSPS at the counter electrode. This counter electrode foil was measured to exhibit a molar ratio of 10:1 (Li:In) with the Li counter electrode. The impedance measurements were performed on a Bio-Logic SP200 instrument at frequencies between 7 MHz and 0.5 Hz using a 5 mV signal amplitude.

SEM Characterization. SEM images of the samples before and after dealloying were collected using a Hitachi SU8230 SEM with an accelerating voltage of 5 kV and a working distance between 2.3 and 10 mm. SEM samples of the materials before cycling were prepared by fabricating a cell inside an Ar-filled glovebox and disassembling the cell to observe the pressed electrodes. Cross-sectional samples of solid-state cells were prepared by manually breaking pellets or by taking fragments from a fractured pellet. EDS analysis was carried out using an accelerating voltage of 30 kV and a working distance of 15 mm. An X-Max^N X-ray detector (Oxford Instruments) was used for EDS analysis. AZtec 2.3 software was used for EDS mapping.

X-ray Diffraction. XRD analysis was carried out using a PANalytical Empyrean instrument with a Cu Kα radiation source ($\lambda_{K\alpha 1}$ =1.54 Å). Chemically alloyed Li−In and Li−Sn samples were placed on a glass slide and sealed underneath a Mylar film within a glovebox to minimize oxidation during X-ray measurements.

FIB Tomography. Tomography of the porous In material was performed in a dual-beam FEI Nova Nanolab 200 FIB/SEM. Porous samples were attached to an SEM stub with conductive carbon tape (Ted Pella, Inc.) and infilled with carbon paint (Ted Pella, Inc.). The reason for infilling the porous electrode samples was twofold: first, it helped with image segmentation to distinguish the pores from the metal,[44] and second, it minimized FIB artifacts like curtaining.[45] The sample was dried under vacuum (0.08 mTorr) for 24 h before tomography. The region of interest (ROI) was coated with a 500 nm thick platinum layer to protect it from Ga^+ ion damage. Additionally, three Pt fiducial markers were deposited on the ROI to assist with the alignment of the image stack.

For serial sectioning of the ROI, three trenches were etched around it and the front face was polished with an ion current of 300 pA. Next, automated serial sectioning software (Auto Slice & View, Thermo Fisher Scientific) was used to section and image the specimen with a tilt of 52°. This tilt causes a visual compression along the *y*-axis, and the *x* and *y* scale bars are adjusted accordingly to obtain the 3D reconstruction (Figure 2b). An accelerating voltage of 5 kV was used for electron beam imaging with a working distance of 5 mm. The slice thickness in the *z* direction was 80 nm, and the ion current used for slicing was 300 pA. Image stacks of 180 images were collected from three randomly chosen regions of the porous In electrode sample. Image alignment was performed in MATLAB using the Pt fiducial markers, and 3D reconstruction of the segmented data was performed using Dragonfly software (Object Research Systems). Estimates of porosity, surface area, volume, and tortuosity were also calculated with Dragonfly. The Dragonfly software computes tortuosity from a three-dimensional reconstruction by reading segmented images in each direction (i.e., *x*, *y*, or *z*) and finding all possible curvilinear and Euclidian paths within the segment. Tortuosity is calculated by computing the quotient of the curvilinear and Euclidian lengths for all segments.

■ ASSOCIATED CONTENT

Supporting Information

The Supporting Information is available free of charge at https://pubs.acs.org/doi/10.1021/acs.chemmater.9b04992.

Additional morphological characterization, effects of different alloying species on porosity formation, characterization of solid-state battery architecture, additional electrochemistry, and investigation of morphological evolution of electrodes with cycling (PDF)

■ AUTHOR INFORMATION

Corresponding Author

Matthew T. McDowell − *George W. Woodruff School of Mechanical Engineering and School of Materials Science and Engineering, Georgia Institute of Technology, Atlanta, Georgia 30332, United States;* orcid.org/0000-0001-5552-3456; Email: mattmcdowell@gatech.edu

Authors

Sang Yun Han − *George W. Woodruff School of Mechanical Engineering, Georgia Institute of Technology, Atlanta, Georgia 30332, United States*

John A. Lewis − *School of Materials Science and Engineering, Georgia Institute of Technology, Atlanta, Georgia 30332, United States*

Pralav P. Shetty − *George W. Woodruff School of Mechanical Engineering, Georgia Institute of Technology, Atlanta, Georgia 30332, United States;* orcid.org/0000-0002-0583-5707

Jared Tippens − *George W. Woodruff School of Mechanical Engineering, Georgia Institute of Technology, Atlanta, Georgia 30332, United States*

David Yeh − *School of Materials Science and Engineering, Georgia Institute of Technology, Atlanta, Georgia 30332, United States*

Thomas S. Marchese − *School of Materials Science and Engineering, Georgia Institute of Technology, Atlanta, Georgia 30332, United States;* orcid.org/0000-0002-3668-5000

Complete contact information is available at: https://pubs.acs.org/10.1021/acs.chemmater.9b04992

Notes

The authors declare no competing financial interest.

■ ACKNOWLEDGMENTS

This work was supported by the Air Force Office of Scientific Research (AFOSR) under Grant FA9550-17-1-0130. J.A.L. acknowledges support from the NASA Space Technology Research Fellowship. A portion of this work is based upon the work supported by the National Science Foundation under Award no. DMR-1652471. This research was performed in part at the Georgia Tech Institute for Electronics and Nanotechnology, a member of the National Nanotechnology Coordinated Infrastructure, which is supported by the National Science Foundation (Grant ECCS-1542174).

■ REFERENCES

(1) Snyder, J.; Fujita, T.; Chen, M. W.; Erlebacher, J. Oxygen Reduction in Nanoporous Metal-Ionic Liquid Composite Electrocatalysts. *Nat. Mater.* **2010**, *9*, 904−907.

(2) Duarte, I.; Ferreira, J. M. F. Composite and Nanocomposite Metal Foams. *Materials* **2016**, *9*, 1−34.

(3) Marx, J.; Portanova, M.; Rabiei, A. Ballistic Performance of Composite Metal Foam against Large Caliber Threats. *Compos. Struct.* **2019**, *225*, No. 111032.
(4) Lang, X.; Hirata, A.; Fujita, T.; Chen, M. Nanoporous Metal/Oxide Hybrid Electrodes for Electrochemical Supercapacitors. *Nat. Nanotechnol.* **2011**, *6*, 232−236.
(5) Bringa, E. M.; Monk, J. D.; Caro, A.; Misra, A.; Zepeda-Ruiz, L.; Duchaineau, M.; Abraham, F.; Nastasi, M.; Picraux, S. T.; Wang, Y. Q.; et al. Are Nanoporous Materials Radiation Resistant? *Nano Lett.* **2012**, *12*, 3351−3355.
(6) Biener, J.; Wittstock, A.; Zepeda-Ruiz, L. A.; Biener, M. M.; Zielasek, V.; Kramer, D.; Viswanath, R. N.; Weissmüller, J.; Bäumer, M.; Hamza, A. V. Surface-Chemistry-Driven Actuation in Nanoporous Gold. *Nat. Mater.* **2009**, *8*, 47−51.
(7) Hu, K.; Lan, D.; Li, X.; Zhang, S. Electrochemical DNA Biosensor Based on Nanoporous Gold Electrode and Multifunctional Encoded DNA-Au Bio Bar Codes. *Anal. Chem.* **2008**, *80*, 9124−9130.
(8) Chen, Q.; Sieradzki, K. Spontaneous Evolution of Bicontinuous Nanostructures in Dealloyed Li-Based Systems. *Nat. Mater.* **2013**, *12*, 1102−1106.
(9) Cook, J. B.; Detsi, E.; Liu, Y.; Liang, Y. L.; Kim, H. S.; Petrissans, X.; Dunn, B.; Tolbert, S. H. Nanoporous Tin with a Granular Hierarchical Ligament Morphology as a Highly Stable Li-Ion Battery Anode. *ACS Appl. Mater. Interfaces* **2017**, *9*, 293−303.
(10) Tao, Y.; Zeng, G.; Xiao, C.; Liu, Y.; Qian, Y.; Feng, J. Porosity Controlled Synthesis of Nanoporous Silicon by Chemical Dealloying as Anode for High Energy Lithium-Ion Batteries. *J. Colloid Interface Sci.* **2019**, *554*, 674−681.
(11) Zinchenko, O.; De Raedt, H. A.; Detsi, E.; Onck, P. R.; De Hosson, J. T. M. Nanoporous Gold Formation by Dealloying: A Metropolis Monte Carlo Study. *Comput. Phys. Commun.* **2013**, *184*, 1562−1569.
(12) Briot, N. J.; Balk, T. J. Developing Scaling Relations for the Yield Strength of Nanoporous Gold. *Philos. Mag.* **2015**, *95*, 2955−2973.
(13) Erlebacher, J.; Karma, A.; Dimitrov, N.; Sieradzki, K.; Aziz, M. J. Evolution of Nanoporosity in Dealloying. *Nature* **2001**, *410*, 450−453.
(14) Jia, F.; Yu, C.; Deng, K.; Zhang, L. Nanoporous Metal (Cu, Ag, Au) Films with High Surface Area: General Fabrication and Preliminary Electrochemical Performance. *J. Phys. Chem. C* **2007**, *111*, 8424−8431.
(15) Wang, C.; Chen, Q. Reduction-Induced Decomposition: Spontaneous Formation of Monolithic Nanoporous Metals of Tunable Structural Hierarchy and Porosity. *Chem. Mater.* **2018**, *30*, 3894−3900.
(16) Coaty, C.; Zhou, H.; Liu, H.; Liu, P. A Scalable Synthesis Pathway to Nanoporous Metal Structures. *ACS Nano* **2018**, *12*, 432−440.
(17) Han, S. Y.; Boebinger, M. G.; Kondekar, N. P.; Worthy, T. J.; McDowell, M. T. Seeded Nanowire and Microwire Growth from Lithium Alloys. *Nano Lett.* **2018**, *18*, 4331−4337.
(18) Lei, D.; Benson, J.; Magasinski, A.; Berdichevsky, G.; Yushin, G. Transformation of Bulk Alloys to Oxide Nanowires. *Science* **2017**, *355*, 267−271.
(19) An, W.; Gao, B.; Mei, S.; Xiang, B.; Fu, J.; Wang, L.; Zhang, Q.; Chu, P. K.; Huo, K. Scalable Synthesis of Ant-Nest-like Bulk Porous Silicon for High-Performance Lithium-Ion Battery Anodes. *Nat. Commun.* **2019**, *10*, 1−11.
(20) Zhao, J.; Zhou, G.; Yan, K.; Xie, J.; Li, Y.; Liao, L.; Jin, Y.; Liu, K.; Hsu, P. C.; Wang, J.; et al. Air-Stable and Freestanding Lithium Alloy/Graphene Foil as an Alternative to Lithium Metal Anodes. *Nat. Nanotechnol.* **2017**, *12*, 993−999.
(21) Yang, Y.; Liu, S.; Bian, X.; Feng, J.; An, Y.; Yuan, C. Morphology- and Porosity-Tunable Synthesis of 3D Nanoporous SiGe Alloy as a High-Performance Lithium-Ion Battery Anode. *ACS Nano* **2018**, *12*, 2900−2908.
(22) Dunlap, N. A.; Kim, J.; Oh, K. H.; Lee, S. H. Slurry-Coated Sheet-Style Sn-Pan Anodes for All-Solid-State Li-Ion Batteries. *J. Electrochem. Soc.* **2019**, *166*, A915−A922.
(23) Obrovac, M. N.; Chevrier, V. L. Alloy Negative Electrodes for Li-Ion Batteries. *Chem. Rev.* **2014**, *114*, 11444−11502.
(24) Webb, S. A.; Baggetto, L.; Bridges, C. A.; Veith, G. M. The Electrochemical Reactions of Pure Indium with Li and Na: Anomalous Electrolyte Decomposition, Benefits of FEC Additive, Phase Transitions and Electrode Performance. *J. Power Sources* **2014**, *248*, 1105−1117.
(25) Weppner, W.; Huggins, R. A. Thermodynamic Properties of the Intermetallic Systems Lithium-Antimony and Lithium-Bismuth. *J. Electrochem. Soc.* **1978**, *125*, 7−14.
(26) He, M.; Kravchyk, K.; Walter, M.; Kovalenko, M. V. Monodisperse Antimony Nanocrystals for High-Rate Li-Ion and Na-Ion Battery Anodes: Nano versus Bulk. *Nano Lett.* **2014**, *14*, 1255−1262.
(27) McDowell, M. T.; Lee, S. W.; Nix, W. D.; Cui, Y. 25th Anniversary Article: Understanding the Lithiation of Silicon and Other Alloying Anodes for Lithium-Ion Batteries. *Adv. Mater.* **2013**, *25*, 4966−4985.
(28) Nitta, N.; Wu, F.; Lee, J. T.; Yushin, G. Li-Ion Battery Materials: Present and Future. *Mater. Today* **2015**, *18*, 252−264.
(29) Liu, N.; Lu, Z.; Zhao, J.; McDowell, M. T.; Lee, H. W.; Zhao, W.; Cui, Y. A Pomegranate-Inspired Nanoscale Design for Large-Volume-Change Lithium Battery Anodes. *Nat. Nanotechnol.* **2014**, *9*, 187−192.
(30) Chae, S.; Choi, S. H.; Kim, N.; Sung, J.; Cho, J. Integration of Graphite and Silicon Anodes for the Commercialization of High-Energy Lithium-Ion Batteries. *Angew. Chem., Int. Ed.* **2020**, *59*, 110−135.
(31) McDowell, M. T.; Xia, S.; Zhu, T. The Mechanics of Large-Volume-Change Transformations in High-Capacity Battery Materials. *Extreme Mech. Lett.* **2016**, *9*, 480−494.
(32) Malik, R.; Loveridge, M. J.; Williams, L. J.; Huang, Q.; West, G.; Shearing, P. R.; Bhagat, R.; Walton, R. I. Porous Metal-Organic Frameworks for Enhanced Performance Silicon Anodes in Lithium-Ion Batteries. *Chem. Mater.* **2019**, *31*, 4156−4165.
(33) Wang, J.; Fan, F.; Liu, Y.; Jungjohann, K. L.; Lee, S. W.; Mao, S. X.; Liu, X.; Zhu, T. Structural Evolution and Pulverization of Tin Nanoparticles during Lithiation-Delithiation Cycling. *J. Electrochem. Soc.* **2014**, *161*, F3019−F3024.
(34) Aurbach, D. Review of Selected Electrode-Solution Interactions Which Determine the Performance of Li and Li Ion Batteries. *J. Power Sources* **2000**, *89*, 206−218.
(35) Lewis, J. A.; Tippens, J.; Cortes, F. J. Q.; McDowell, M. T. Chemo-Mechanical Challenges in Solid-State Batteries. *Trends Chem.* **2019**, *1*, 845−857.
(36) Cheng, E. J.; Sharafi, A.; Sakamoto, J. Intergranular Li Metal Propagation through Polycrystalline $Li_{6.25}Al_{0.25}La_3Zr_2O_{12}$ Ceramic Electrolyte. *Electrochim. Acta* **2017**, *223*, 85−91.
(37) Lewis, J. A.; Cortes, F. J. Q.; Boebinger, M. G.; Tippens, J.; Marchese, T. S.; Kondekar, N.; Liu, X.; Chi, M.; McDowell, M. T. Interphase Morphology between a Solid-State Electrolyte and Lithium Controls Cell Failure. *ACS Energy Lett.* **2019**, *4*, 591−599.
(38) Santhosha, A. L.; Medenbach, L.; Buchheim, J. R.; Adelhelm, P. The Indium−Lithium Electrode in Solid-State Lithium-Ion Batteries: Phase Formation, Redox Potentials, and Interface Stability. *Batteries Supercaps* **2019**, *2*, 524−529.
(39) Tippens, J.; Miers, J. C.; Afshar, A.; Lewis, J. A.; Cortes, F. J. Q.; Qiao, H.; Marchese, T. S.; Di Leo, C. V.; Saldana, C.; McDowell, M. T. Visualizing Chemomechanical Degradation of a Solid-State Battery Electrolyte. *ACS Energy Lett.* **2019**, *4*, 1475−1483.
(40) Wu, X.; Billaud, J.; Jerjen, I.; Marone, F.; Ishihara, Y.; Adachi, M.; Adachi, Y.; Villevieille, C.; Kato, Y. Operando Visualization of Morphological Dynamics in All-Solid-State Batteries. *Adv. Energy Mater.* **2019**, *9*, No. 1901547.
(41) Delattre, B.; Amin, R.; Sander, J.; Coninck, D.; Tomsia, A. P.; Chiang, Y. Impact of Pore Tortuosity on Electrode Kinetics in

https://dx.doi.org/10.1021/acs.chemmater.9b04992
Chem. Mater. XXXX, XXX, XXX−XXX

Lithium Battery Electrodes : Study in Directionally Freeze-Cast $LiNi_{0.8}Co_{0.15}Al_{0.05}O_2$ (NCA). *J. Electrochem. Soc.* **2018**, *165*, A388−A395.
(42) Chen-Wiegart, Y. K.; Demike, R.; Erdonmez, C.; Thornton, K.; Barnett, S. A.; Wang, J. Tortuosity Characterization of 3D Microstructure at Nano-Scale for Energy Storage and Conversion Materials. *J. Power Sources* **2014**, *249*, 349−356.
(43) Bron, P.; Johansson, S.; Zick, K.; Der Günne, J. S. A.; Dehnen, S.; Roling, B. $Li_{10}SnP_2S_{12}$: An Affordable Lithium Superionic Conductor. *J. Am. Chem. Soc.* **2013**, *135*, 15694−15697.
(44) Vierrath, S.; Güder, F.; Menzel, A.; Hagner, M.; Zengerle, R.; Zacharias, M.; Thiele, S. Enhancing the Quality of the Tomography of Nanoporous Materials for Better Understanding of Polymer Electrolyte Fuel Cell Materials. *J. Power Sources* **2015**, *285*, 413−417.
(45) Aitkaliyeva, A.; Madden, J. W.; Miller, B. D.; Cole, J. I. Implementation of Focused Ion Beam (FIB) System in Characterization of Nuclear Fuels and Materials. *Micron* **2014**, *67*, 65−73.

https://dx.doi.org/10.1021/acs.chemmater.9b04992
Chem. Mater. XXXX, XXX, XXX−XXX